Aston University

MSc by Research

Fluid, heat and mass transfer in a Venlo type greenhouse with variable boundary conditions

Author:
Nerupa Kidnapillai

Supervisors:
Dr. Sotos Generalis
Dr. Takeshi Akinaga

October 2013

Abstract

Greenhouse production of crops is problematic in the United Arab Emirates due to the harsh arid climate, which produces an unfavourable micro-climate within a greenhouse. This 'micro-climate' is controlled to create optimal conditions to grow crops. In order to determine these conditions, we simulate a two-dimensional micro-climate to study the temperature distribution of a ventilated system with different outlet positions. Thus creating the symmetric and asymmetric models. These models are compared between two cases of fluid properties defined by nondimensional parameters such as the Reynolds number. The aim is to understand how to amend the conditions of a micro-climate to remove heat by ventilation, as well as to determine which model is ventilated better by comparing models across cases. Our objectives are to observe the behaviour of the airflow for each model by evaluating heat balances, and then analyse whether the positioning of the outlet effects heat transfers in accordance to different fluid properties. The finite-difference method is presented for the numerical solution of the Navier-Stokes equations of an incompressible Newtonian fluid, in two dimensions, a stream function-vorticity formulation. Using a uniform grid of mesh points to discretise these equations, we then derive finite difference equations which are then solved to approximate solutions.

Numerical results show that the symmetric model for the set of parameters (case 2) with Reynolds number $Re = 1.622 \times 10^5$ and Grashof number $Gr = 6.770 \times 10^9$ as the most influential case in the distribution of temperature. Thus, overall there is a better ventilated system through the symmetric channel for case 2. This is highlighted by a total heat flux of $Q = 54.90$ with a ratio of averaged gradient between the ground and the roof as $6.272 : 1$.

Keywords: Greenhouse, ventilation, heat and mass transfer, Navier-Stokes equations, stream function-vorticity formulation, finite difference approximation

Acknowledgements

I would like to thank my supervisor Dr Sotos Generalis, and the Mathematics staff for their support. Also for his supervisory role I would like to express my deepest appreciation to Dr Takeshi Akinaga who has made the writing of this thesis achievable through this guidance and encouragement. In addition I must thank Dr Laura Rebollo-Neira for her suggestions which has helped make improvements to this project.

I am truly thankful for the advice, patience and great friendships from Chloé Seivwright, Amie Fasuluku, Uche Ogeah, Larry Godwin, Elizabeth Harrison and Jack Freeman. Furthermore, the completion of this project would not have been possible without their constant support for which I am eternally grateful. I would also like to thank Maria and Eduardo for their kindness and support.

Finally I would like to give special acknowledgement to my family, in particular my parents, I thank them for giving me the strength to succeed. For without them, I would not have been able to continue with my studies.

Contents

List of Figures

Nomenclature

t	–	Time
x, y, z	–	Cartesian coordinates
$\hat{\boldsymbol{i}}, \hat{\boldsymbol{j}}, \hat{\boldsymbol{k}}$	–	Unit vectors in the Cartesian coordinates system
$\boldsymbol{n}$	–	Unit vector normal to wall
∇	–	Gradient operator: $\boldsymbol{i}\frac{\partial}{\partial x} + \boldsymbol{j}\frac{\partial}{\partial y} + \boldsymbol{k}\frac{\partial}{\partial z}$ for three dimensional description
	–	Gradient operator: $\boldsymbol{i}\frac{\partial}{\partial x} + \boldsymbol{j}\frac{\partial}{\partial y}$ for two dimensional description
∇^2	–	Laplacian operator: $\frac{\partial^2}{\partial x^2} + \frac{\partial^2}{\partial y^2} + \frac{\partial^2}{\partial z^2}$ for three dimensional description
	–	Laplacian operator: $\frac{\partial^2}{\partial x^2} + \frac{\partial^2}{\partial y^2}$ for two dimensional description
$\triangle_2$	–	Laplacian operator for two dimensional system $(x - y)$: $\frac{\partial^2}{\partial x^2} + \frac{\partial^2}{\partial y^2}$
ρ	–	Density of fluid
μ	–	Viscosity of fluid
ν	–	Kinematic viscosity of fluid (μ/ρ)
λ	–	Thermal conductivity
α	–	Thermal expansion coefficient
κ	–	Thermal diffusion coefficient
$\boldsymbol{g}$	–	Acceleration vector due to gravity
g	–	Acceleration due to gravity $(\lvert\boldsymbol{g}\rvert)$
$\boldsymbol{u}$	–	Velocity vector
u, v, w	–	Velocity components
p	–	Pressure
T	–	Temperature
$\boldsymbol{\omega}$	–	Vorticity $(\nabla \times \boldsymbol{u})$
ω	–	z component of vorticity $(\boldsymbol{\omega} \cdot \boldsymbol{k})$
ψ	-	Stream function defined on $x - y$ plane $(u = \partial\psi/\partial y, v = -\partial\psi/\partial x)$
γ	–	Relaxation factor
Gr	–	Grashof number
Pr	–	Prandtl number
Re	–	Reynolds number

Chapter 1

Introduction

In this project we study fluid flow phenomena of a greenhouse. The environment of a greenhouse is considered problematic when creating desired conditions to cultivate crops, particularly in arid climates. The harsh environment within a greenhouse is explored through a two-dimensional analysis by creating a modelled 'micro-climate'. We will explore how to control the temperature conditions within a micro-climate through ventilation, by heat and mass transfers with variable boundary conditions.

1.1 Motivation

A greenhouse is a building commonly used for the cultivation of crops such as, lettuce, pepper and tomatoes. This involves growing crops under a controlled environment by creating favourable conditions, thus generating a micro-climate. The main objective is to achieve sustainable growth by efficient means of production all year round. We note that a successful cultivation of crops is generated through high quality yields. Subsequently this creates many benefits to the economy, such as the capacity to reduce the rate of imported food by the creation of a sustainable agriculture sector. Simultaneously, the reduction of environmental externalities would be brought by the sustainable development of greenhouse crop production. There are various trends in greenhouse systems which reflect upon the climatic conditions of specific regions. It has been highlighted by Zabeltitz (2011) that there are several climatic elements to be considered such as: solar radiation, temperature, precipitation, humidity, evaporation, and wind veloc-

ity. These elements affect the type of greenhouse system used to determine an optimal micro-climate for growing crops. For example, the Mediterranean climate is characterised as warm to hot, with dry summers and wet winters. Thus, a greenhouse cooling system is implemented as Sapounas et al. (2008) stated that the main techniques used are based upon ventilation and shading, through fans and pads. However there are many limitations and problems incurred by implementing these cooling techniques to create an appropriate micro-climate, particularly during hot periods of the year. This yields further stipulation across other climates that are mainly hot and dry all year round, which is the case in this particular project. Furthermore Sethi and Sharma (2007) suggests that unlike the heating system which is well established and straightforward, greenhouse cooling systems are considered problematic. Therefore in order to generate adequate ventilation to create the desired micro-climate, it is important to understand the thermal behaviour of a greenhouse. For that reason, the focal point of this research is to understand how changing the properties of the fluid affects heat balances within a micro-climate.

1.2 The Problem

Davies (2005) highlights that sunlight provides the primary energy for photosynthesis, the food chain and all human nutrition. However intense sunlight induces high temperatures, which can restrict or prevent cultivation of many crops. This is the case in arid countries such as the United Arab Emirates (UAE), where temperatures reach well over 40 °C in the summer. This project is concerned with the problems incurred when creating desired conditions of a micro-climate of a greenhouse in the UAE. This type of climate is described by Böer (1997) and it is explained that the limited amount of freshwater, combined with extremely high summer temperatures, and high evaporation rates produces a harsh environment for vegetation to grow. The significance of greenhouse technology in agriculture is also highlighted by a growing population and the heavy dependence upon importing agricultural commodities. Moreover there is a clear problem which is emphasised by Kumar et al. (2009), seeing that the development of a suitable cooling system that provides a congenial micro-climate for crop growth is a difficult task,

as the design is closely related to the local environmental conditions. Although there have been many developments of greenhouse systems such as, solar-powered systems and seawater greenhouse systems. These are predominantly based upon cooling techniques, which is usually problematic when seeking to control the thermal conditions of a micro-climate because of the harsh climatic conditions. Experimental work is crucial in the study of a micro-climate of a greenhouse, however it is costly and very time consuming. In addition, experimental work entails many factors that determine a suitable environment for a greenhouse, such as the geometry of a greenhouse, climatic conditions, the ventilation rate, plant activity, solar radiation, air flow etc. Therefore by considering only a few fundamental factors that influences a micro-climate, we are able to take a numerical approach to study the phenomena of a greenhouse. Thus we simplify the problem by focusing our attention upon the ventilation within a greenhouse. There are several different forms ranging between natural and forced ventilation, this research has adopted forced ventilation by mathematically modelling a wind-driven system through the parameters within our calculations.

This type of approach has become an innovation of many research endeavours, in which the field of fluid dynamics is used to create mathematical models aimed to simulate the micro-climate of a greenhouse. Despite the limitations of the applicability of these studies upon real world solutions, due to the simplification of the problem, computational fluid dynamics (CFD) is used as a fundamental numerical approach to create models in order to study these types of fluid flow related phenomena. Nevertheless we are able to obtain critical information by studying the flow patterns inside the greenhouse through the simulated micro-climate. This approach has been utilised to model a micro-climate in order to apply a ventilation system, and determine how the variation of parameters influence the behaviour of the fluid flows, as well as heat and mass transfers in a greenhouse. In order to develop a micro-climate with favourable conditions to produce a viable greenhouse system in the UAE, it is fundamental to have an understanding of the behaviour of this fluid flow phenomena.

1.3 Goals and outline

A two dimensional study has been taken to observe the behaviour of the airflow within a micro-climate of a greenhouse with variable boundary conditions. This entails using the Navier-Stokes equations to model this fluid flow, furthermore by a transformation of these equations we are able to derive the stream function-vorticity formulation. The finite difference method is employed whereby a finite difference mesh has been applied to discretise the governing equations to approximate the derivatives on a set of discrete data points. Moreover, through the application of CFD we are able to control parameters within our calculations to create two different cases. These cases are analysed in regards to two distinct models. The configurations of these models have been adapted from the greenhouse depicted by Davies and Paton (2005), as well as the design of a Venlo type greenhouse. Thus the goal of this project is to compare two models with different outlet positions for two different cases. The cases are defined by the following parameters; Prandtle number, Reynolds number, Grashof number, mesh size, and time step. The evaluation of the behaviour of airflow is fundamental to the goal of this project, such that the following variables will be analysed; temperature (T), stream function (ψ) and vorticity (ω). The motivation of this project is to understand how to amend the conditions of a micro-climate mainly to remove heat by ventilation, which is determined by the evaluation of heat balances between the models control parameters. This project is presented in the following order to unfold how the research problem has been carried out. Chapter 2 describes the research problem in greater detail through the formulation of mathematical model. Following this, the numerical method used to solve the problem is described in chapter 3. Moreover, the results are then presented and discussed in chapter 4. Furthermore conclusions are drawn and potential further work is deemed in chapter 5.

Chapter 2

The research problem

This chapter looks at how the physical problem is mathematically modelled to create a simulated micro-climate of a Venlo type greenhouse. The construction of the two models will be discussed. Furthermore the mathematical formulation used to model the flow field is examined as we derive the governing equations of our problem.

2.1 Formulation of the problem

In order to simulate a micro-climate of a greenhouse we have adapted the Seawater Greenhouse model which has been constructed in the UAE and applied by Davies and Paton (2005). Only the basic dimensions of this particular greenhouse design has been applied, since it represents a typical greenhouse in the UAE. Furthermore the greenhouse model considered is concerned with the case of a wind driven ventilation system. A fan is positioned at the inlet to ventilate the greenhouse as air flows towards the outlet.

We explore the phenomena of fluid flows within the micro-climate of this greenhouse design through a two-dimensional analysis. Therefore we consider a vertical cross section which is positioned in the lengthwise mid-plane, perpendicular to the base of a Venlo type greenhouse shown by Figure (2.1). The main parameters that relate to this model are summarised in Table (2.1). The Venlo greenhouse is a well known structure used for the cultivation of crops. Given that it has a wide range of characteristics that make it suitable for growing a vast variety of crops in most climate conditions. The number of

physical factors that characterises this greenhouse is minimised in order to comprehend a simpler two-dimensional case. This allows us to manipulate the environment of the modelled micro-climate.

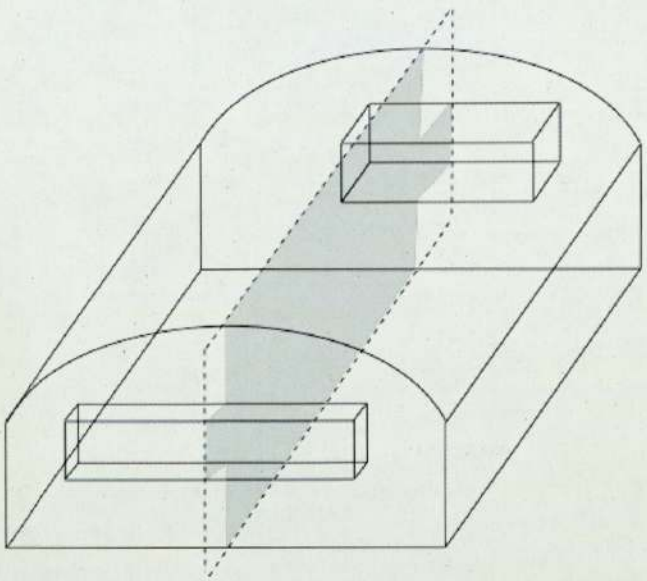

Figure 2.1: Basic geometric configuration of a Venlo type greenhouse in which the two-dimensional models are created from.

Table 2.1: Basic design parameters

Width(m)	18
Length(m)	42
Maximum height(m)	5.5
Air flow(m^3/s)	15
Average air flow (m/s)	0.625
Dimensions (width $\times$ height $\times$ thickness):	
Inlet, fan (m)	$12 \times 2 \times 2$
Outlet(m)	$8 \times 2 \times 4$

Through controlling the parameters within our calculations, we are able to observe how heat and mass transfers are affected by variable boundary conditions. We vary the positioning of the outlet to create two separate models that simulate the micro-climate of this greenhouse. The first model is illustrated by Figure (2.2) in which both the inlet and outlet channels are connected to the greenhouse with the same height above the ground ($1.75m$). The model is symmetric in the horizontal direction. The second model is asymmetric shown in Figure (2.3), which has been created by raising the positioning of the outlet by one metre (now $2.75m$ above the ground), while maintaining the posi-

tion of the inlet. The coordinate system is outlined and the orientation axes in relation to the physical problem is shown in both the figures below. We take x, y as Cartesian coordinates in the horizontal and vertical directions (with unit vectors, $\hat{\boldsymbol{i}}, \hat{\boldsymbol{j}}$ respectively).

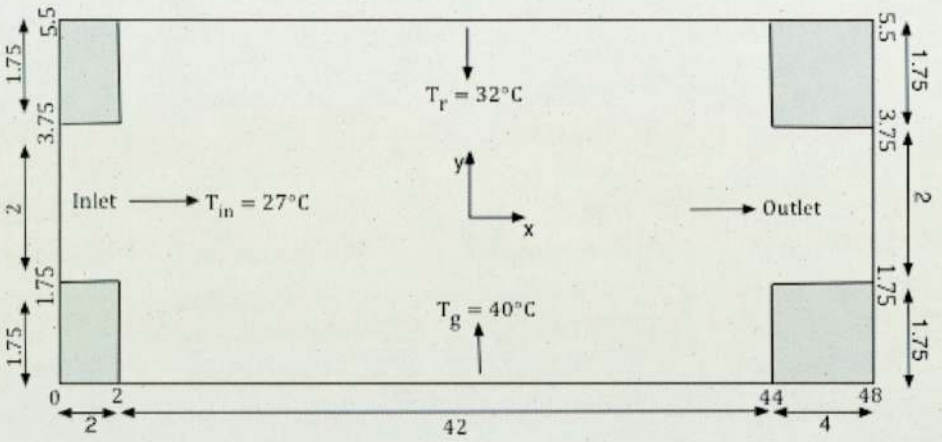

Figure 2.2: Model 1 - Symmetric channel with inlet and outlet positioning (m)

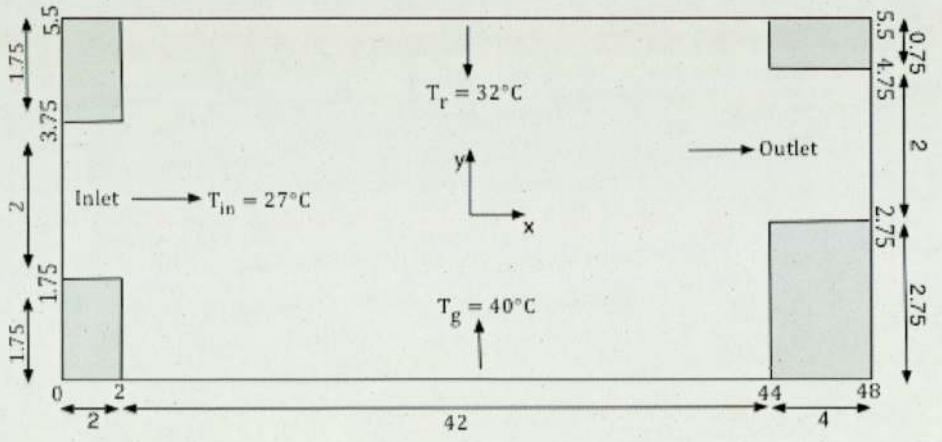

Figure 2.3: Model 2 - Asymmetric channel with inlet and outlet positioning (m)

The temperature conditions involved (typical climate for UAE) for both models remain constant throughout this study and are defined at the ground ($T_g = 40\,°\text{C}$), roof ($T_r = 32\,°\text{C}$) and inlet ($T_{in} = 27\,°\text{C}$). In addition the walls of these models along the shaded regions are insulated in order to observe the heat flux between the defined physical system. For the purpose of this project, the velocity profile representing the ventilation of airflow is modelled by the Poiseuille profile at the inlet as a boundary condition in order to simplify the problem. Two different ventilation rates will be explored 0.01 m/s and 1 m/s though two cases. This is done in order to monitor the differences or similarities of temperature balances between these two cases among the two models.

Our fundamental focus is to observe the emerging patterns of airflow between these modelled micro-climates. Torre-Gea et al. (2011) states that a micro-climate is a highly complex system in which the airflow and the variables that create the climate behave in a temporal and non-linear manner. This is expressed through a system of complex second-order differential equations which cannot be solved analytically. We therefore describe the greenhouse phenomena through the Navier-Stokes equations and the Energy equations.

2.2 Governing equations

In this section we provide the mathematical formulation to model our fluid flow. We assume an incompressible flow of a Newtonian fluid, where stress is proportional to shear rate and the density of the fluid with respect to time and space is constant. It is important to note that we observe the motion of fluid (as a function) at time t and position $\boldsymbol{x}$ in space, which yields an Eulerian representation of the flow field. Therefore we represent the velocity vector field as $\boldsymbol{u}(\boldsymbol{x}, t)$, the fluid density $\rho(\boldsymbol{x}, t)$, and the pressure field $p(\boldsymbol{x}, t)$ (Doering and Gibbon, 1995).

Fluids obey the general laws of continuum mechanics: conservation of mass, momentum, and energy (Foias et al., 2001).

The conservation of mass is expressed by the following continuity equation,

$$\frac{\partial \rho}{\partial t} + \nabla \cdot (\rho \boldsymbol{u}) = 0. \tag{2.1}$$

Given that we are examining incompressible Newtonian fluids, such that density is assumed constant in space and time $\rho(\boldsymbol{x}, t) = \rho_0$. Hence the continuity equation is reduced to the divergence free condition $\nabla \cdot \boldsymbol{u} = 0$, known as the incompressibility condition.

The conservation of momentum implied by Newton's law of motion along with the continuity equation is used to derive the following general Navier-Stokes equation,

$$\rho \left[\frac{\partial \boldsymbol{u}}{\partial t} + (\boldsymbol{u} \cdot \nabla) \boldsymbol{u} \right] = -\nabla p + \mu \nabla^2 \boldsymbol{u} - \rho \boldsymbol{g}, \tag{2.2}$$

for the velocity vector $\boldsymbol{u}$, pressure p, and density ρ which is now a parameter.

Given that this project is concerned with the problem of thermal convection (heat and mass transfer) of an incompressible Newtonian fluid. Such that, the influence of the temperature field on the incompressible fluid's motion is taken into account by introducing a buoyancy force, Doering and Gibbon (1995). Therefore we apply the Boussinesq approximation which observes that, the variations of density can be ignored except for when they are multiplied by the acceleration of gravity in Equation (2.2) for the vertical component of the velocity vector, Zeytounian and Mecanique (2003) cites the work of Boussinesq (1903). Subsequently the variation in temperature usually leads to density variations, where the Boussinesq approximation gives rise to buoyancy forces through the equation of states,

$$\rho = \rho_0 \left[1 - \alpha (T - T_r) \right], \tag{2.3}$$

α is the coefficient of thermal expansion. If we now write $(T - T_r)$ as T, in the equation above we get,

$$\rho = \rho_0 - \rho_0 \, \alpha T. \tag{2.4}$$

We are then able to deduce the following Boussinesq equations for velocity vector $\boldsymbol{u}$, pressure p, and temperature $T(\boldsymbol{x}, t)$ of the fluid:

$$\rho_0 \left[\frac{\partial \boldsymbol{u}}{\partial t} + (\boldsymbol{u} \cdot \nabla) \boldsymbol{u} \right] = -\nabla p + \mu \nabla^2 \boldsymbol{u} + g\alpha T \hat{\boldsymbol{j}}, \tag{2.5}$$

$$\nabla \cdot \boldsymbol{u} = 0, \tag{2.6}$$

$$\frac{\partial T}{\partial t} + (\boldsymbol{u} \cdot \nabla) T = \kappa \nabla^2 T. \tag{2.7}$$

By introducing the acceleration of gravity as $-\hat{\boldsymbol{j}} g$, where $\hat{\boldsymbol{j}}$ is the unit vector in the vertical direction taken as the y-direction, the reference temperature as T_r and the reference density as ρ_0; the Navier-Stokes equations are now represented by Equations (2.5) and (2.6). We also derive the energy equation in (2.7), which incorporates the conservation of energy and is ultimately the convection-diffusion equation for the temperature field; where κ represents the thermal diffusion coefficient.

2.2.1 Nondimensional equations

The nondimensional forms of our governing equations are established for the purpose of universal applicability. We are able to normalise every parameter using a reference constant so that they are not associated with a physical dimension. Such that a dimensionless variable can be defined as:

$$a^* = \frac{a}{A},$$

with a being a variable which has a dimension (unit of measure), A is the reference constant, and a^* is denoted as the non-dimensional variable. Furthermore the Equations (2.8) - (2.10) are obtained by employing the reference constants from Table (2.2) in order to reduce the number of variables into fewer manageable parameters. Such that we reduce the governing equations to four equations with four unknowns, velocity components (u, v), pressure p, and temperature T.

Table 2.2: Reference constants

Characteristic velocity	U
Characteristic length	L
Reference temperature	T_r
Characteristic time scale	$\frac{L}{U}$
Temperature scale	$T_g - T_r$

$$\frac{\partial \boldsymbol{u}^*}{\partial t^*} ,+(\boldsymbol{u}^* \cdot \nabla^*)\boldsymbol{u}^* = -\nabla^* p* + \frac{1}{Re}\nabla^{*^2}\boldsymbol{u}^* + \frac{Gr}{(Re)^2} T^* \hat{\boldsymbol{j}}, \tag{2.8}$$

$$\nabla^* \cdot \boldsymbol{u}^* = 0, \tag{2.9}$$

$$\frac{\partial T^*}{\partial t^*} + (\boldsymbol{u}^* \cdot \nabla^*)T^* = \frac{1}{Pr\, Re}\nabla^{*^2} T^*. \tag{2.10}$$

Where $Gr = \frac{g\alpha\Delta T L^3}{\nu^2}$, $Re = \frac{UL}{\nu}$ and $Pr = \frac{\nu}{\kappa}$. Equations (2.8-2.10) represent the momentum, incompressibility condition and energy equations respectively. Moreover, the nondimensionalisation of the Navier-Stokes equations and the energy equation is carried out in Appendix A.

2.2.2 Stream function-vorticity formulation

The equations of the problem are reduced further by transforming the Navier-Stokes equations through the velocity-vorticity formulation. We now deal with the continuity equation and the two momentum equations as pressure is eliminated from the governing equations through cross differentiation. We then are able to formulate the stream function - vorticity formulation by combining the definition of the stream function and the velocity-vorticity formulation. Loukopoulos et al. (2013) concludes that for two-dimensional problems there is only one vorticity component (ω) and the two velocity components, $\boldsymbol{u} = (u, v)$ substituted by the stream function, $\psi(x, y)$ defined by

$$u = \frac{\partial \psi}{\partial y}, \qquad v = -\frac{\partial \psi}{\partial x}. \tag{2.11}$$

Thus the velocity-vorticity approach is generally known as the stream function-vorticity approach. Therefore we are now left with following three equations and three unknowns, vorticity ω, stream function ψ, and temperature T

1. Poisson equation

$$\omega = -\nabla^2 \psi, \tag{2.12}$$

2. vorticity transport equation

$$\frac{\partial \omega}{\partial t} + \frac{\partial \psi}{\partial y}\frac{\partial \omega}{\partial x} - \frac{\partial \psi}{\partial x}\frac{\partial \omega}{\partial y} = \frac{1}{Re}\nabla^2 \omega + \frac{Gr}{Re^2}\frac{\partial T}{\partial x}, \tag{2.13}$$

3. stream function formulation of the energy equation

$$\frac{\partial T}{\partial t} + \frac{\partial \psi}{\partial y}\frac{\partial T}{\partial x} - \frac{\partial \psi}{\partial x}\frac{\partial T}{\partial y} = \frac{1}{Pr\,Re}\nabla^2 T. \tag{2.14}$$

Chapter 3

Numerical method

Finite difference methods offer a powerful technique for the solution of heat transfer problems, (Croft and Lilley, 1977). This chapter will discuss how finite difference methods are used to discretise the governing equations to find approximated solutions. Furthermore we develop our computational model in efforts to predict heat and mass transfers within our modelled micro-climate. The fluid flow is characterised by control parameters such as Reynolds number and Grashof number, these will be determined to mathematically model the fluid flow.

3.1 Discretisation by finite difference approximation

In this project we are concerned with the numerical solution of the governing equations (2.12) - (2.14) that models our fluid flow. The finite difference method (FDM) is a numerical method used to discretise these equations, and approximate the derivatives on a set of discrete data points. Consequently the computational domain is discretised in order to use this numerical approach. Since the FDM is applied by first defining a mesh size to construct a grid of spatial points at which each unknown variable is to be sampled. Such that the x-axis and the y-axis are discretised into finite points x_i for $i = 0, ..., n$, and y_j for $j = 0, ..., m$, in which the spacing between the neighbouring points are denoted as Δx and Δy. Furthermore, through discretisation a truncation error is incorporated by the difference between the approximated and actual solutions. The relationship between the derivatives and finite differences are derived by the Taylor

expansion such that,

$$f(x+\Delta x) = f(x) + \frac{df}{dx}(x)\Delta x + \frac{1}{2!}\frac{d^2f}{dx^2}(x)(\Delta x)^2 + ... \tag{3.1}$$

There are three types of approaches to implement the FDM, and for first order approximations the centered, forward, and backward forms are given below, respectively,

$$\frac{df}{dx} = \frac{f_{i+1} - f_{i-1}}{2\Delta x} + \mathcal{O}\big((\Delta x)^2\big), \tag{3.2}$$

$$\frac{df}{dx} = \frac{f_{i+1} - f_i}{\Delta x} + \mathcal{O}(\Delta x), \tag{3.3}$$

$$\frac{df}{dx} = \frac{f_i - f_{i-1}}{\Delta x} + \mathcal{O}(\Delta x), \tag{3.4}$$

where Δx = mesh size and $f_i = f(x_i)$. Additionally $\mathcal{O}(\Delta x)$ is the error proportionality of Δx. In regards to our system of equations, we implement the centered approach to approximate second order derivatives as it is considered to be a better estimate,

$$\frac{d^2f}{dx^2} = \frac{f_{i+1} - 2\,f_i + f_{i-1}}{(\Delta x)^2} + \mathcal{O}\big((\Delta x)^2\big). \tag{3.5}$$

Therefore through the discretisation of the Poisson equation (2.12), vorticity transport equation (2.13), stream function formulation of the energy equation (2.14) we derive the following respectively,

$$\omega_{i,j} = -\frac{\psi_{i+1,j} - 2\psi_{i,j} + \psi_{i-1,j}}{\Delta x^2} - \frac{\psi_{i,j+1} - 2\psi_{i,j} + \psi_{i,j-1}}{\Delta y^2}, \tag{3.6}$$

$$\begin{aligned}\frac{\omega^{k+1} - \omega^k}{\Delta t} &+ \frac{\psi_{i,j+1} - \psi_{i,j-1}}{2\Delta y}\frac{\omega_{i+1,j} - \omega_{i-1,j}}{2\Delta x} \\ &- \frac{\psi_{i+1,j} - \psi_{i-1,j}}{2\Delta x}\frac{\omega_{i,j+1} - \omega_{i,j-1}}{2\Delta y} \\ &= \frac{1}{Re}\left(\frac{\omega_{i+1,j} - 2\omega_{i,j} + \omega_{i-1,j}}{\Delta x^2} + \frac{\omega_{i,j+1} - 2\omega_{i,j} + \omega_{i,j-1}}{\Delta y^2}\right) \\ &+ \frac{Gr}{(Re)^2}\frac{T_{i+1,j} - T_{i-1,j}}{2\Delta x},\end{aligned} \tag{3.7}$$

$$\begin{aligned}\frac{T^{k+1} - T^k}{\Delta t} &+ \frac{\psi_{i,j+1} - \psi_{i,j-1}}{2\Delta y}\frac{T_{i+1,j} - T_{i-1,j}}{2\Delta x} \\ &- \frac{\psi_{i+1,j} - \psi_{i-1,j}}{2\Delta x}\frac{T_{i,j+1} - T_{i,j-1}}{2\Delta y} \\ &= \frac{1}{PrRe}\left(\frac{T_{i+1,j} - 2T_{i,j} + T_{i-1,j}}{\Delta x^2} + \frac{T_{i,j+1} - 2T_{i,j} + T_{i,j-1}}{\Delta y^2}\right).\end{aligned} \tag{3.8}$$

We then solve these finite difference equations (FDEs) for our three unknowns , stream function ψ, vorticity ω, and temperature T. To obtain the next states (ω^{k+1}, T^{k+1}) from the current approximation (ω^k, ψ^k, T^k), we integrate with respect to time. Therefore Equation (3.7) is integrated in the following manner,

$$\omega^{k+1} = \omega^k + \Delta t F(\omega^k, \psi^k, T^k). \tag{3.9}$$

In order to achieve the temperature field, we utilise the procedure in Equation (3.9) for Equation (3.8). To solve for the stream function, we apply the successive over-relaxation method described in the following subsection for Equation (3.6).

3.1.1 Successive over-relaxation method

The implementation of the FDM has transformed Equation (2.12) into Equation (3.6). We then solve approximately for ψ_{ij} to find,

$$\psi_{i,j} = \frac{1}{2(\Delta x^2 + \Delta y^2)} \Bigg((\Delta x^2)(\Delta y^2)\omega_{i,j} + (\psi_{i+1,j} + \psi_{i-1,j})(\Delta y^2) + (\psi_{i,j+1} + \psi_{i,j-1})(\Delta x^2) \Bigg). \tag{3.10}$$

This expression tells us that every stream function sample ($\psi_{i,j}$) is linearly dependent on its four nearest neighbouring points, this creates a linear system of equations. The solution all over (i, j) can be represented as a matrix-vector equation, $A\boldsymbol{x} = \boldsymbol{b}$. This would be achieved by defining vector $\boldsymbol{x}$ to contain all the data points sampled within the domain ($\psi_{i,j}$), matrix A would then express the linear relationship between these points, and vector $\boldsymbol{b}$ defined by the boundary conditions and vorticity function ($\omega_{i,j}$). Generally, this direct method is used to solve such problems by inverting matrix A. However to reduce computational costs we use the successive over relaxation method (SORM). The SORM is a numerical method used to solve linear systems of equations through an iterative process. This results in faster convergence due to the iterative process entailed from the Gauss-Seidel Method (GSM) and Jacobi Method. SORM takes the form of a weighted average between the previous iterate and the computed GSM iterate successively for each component. This weighted average is known as the relaxation factor (γ), and when optimised it leads to the most expedient convergence of an approximated solution. Using the concept of approximating the next step (${\psi_{ij}}^{n+1}$) by incorporating the previous step (${\psi_{ij}}^{n}$) and the approximated solution from the iterative scheme (${\widetilde{\psi_{ij}}}^{n}$), which is taken from Equation (3.10). Therefore we have

$${\psi_{ij}}^{n+1} = {\psi_{ij}}^{n} + \gamma \left({\widetilde{\psi_{ij}}}^{n} - {\psi_{ij}}^{n} \right). \tag{3.11}$$

Since the SORM is applied, the condition that $1 < \gamma < 2$ is enforced, and so we have set $\gamma = 1.05$. We calculate Equation (3.11) for all points within the domain until convergence. In this current study we repeat this process ten times in order to derive

satisfactory solutions, such that the relative error within each iteration should be smaller than the value 10^{-8} in order to verify that the solution is acceptable.

3.2 Control parameters

The computational model has been created from the research problem itself and the numerical method implemented to solve it. We have established two models that were presented in Figures (2.2) - (2.3), for which two cases have been created to explore the behaviour of the airflow. The two cases are shown in Table (3.1), and are distinguished by the control parameters used in the governing equations. The values of these parameters were chosen to represent different fluid flows in which the two different ventilation rates have been implied (0.01 m/s and 1 m/s).

The Prandtl number (Pr) is defined as the ratio of kinetic viscosity to thermal diffusivity of the fluid,

$$Pr = \frac{\nu}{\kappa}, \tag{3.12}$$

in the present study we selected air so that $Pr = 0.71341$.

The Reynolds number (Re) characterises different flow regimes by how fast a fluid flows,

$$Re = \frac{U\,L}{\nu}. \tag{3.13}$$

In this present project we study the following cases, $Re = 1.6224 \times 10^3$ for case 1 and $Re = 1.6224 \times 10^5$ for case 2.

The third nondimensional parameter in our formulation is the Grashof Number (Gr) defined as,

$$Gr = \frac{g\,\alpha\,\Delta T\,L^3}{\nu^2}. \tag{3.14}$$

The Grashof numbers, $Gr = 6.7696 \times 10^5$ and $Gr = 6.7696 \times 10^9$ are used for cases 1 and 2, respectively.

We are able to apply this through the two-dimensional flow field determined by our discretised governing equations (3.6 - 3.8). The Stream Function ψ, is represented by

streamlines that show the direction the fluid will travel in at any point in time. The vorticity (ω), represents the local spin/rotation of a fluid. And temperature (T) incorporates many aspects taken into account surrounding the study of heat transfers. All of which influences the physical property of the fluid in question, thus allowing us to study the airflow within a micro-climate.

Table 3.1: Control parameters specified for each case.

	Case 1	Case 2
Pr	0.71341	0.71341
Re	1.6224×10^3	1.6224×10^5
Gr	6.7696×10^5	6.7696×10^9

3.3 Convergence check

The mesh size has been set to $\Delta x = \Delta y$ for both models, which creates a uniform grid of mesh points (data points). Time-intervals have been taken to create the grid of mesh points at repeated time-steps (Δt). There are many concepts to identify Δt, but since we are solving elliptic type equations we use $\Delta t = (\Delta x)^2 \times c$ for $0 < c < 1$. The general concept to obtain the best approximation for a solution is found by using a sufficiently small mesh. In order to verify this concept, we have successfully completed a convergence check in which the mesh size $\Delta x = \frac{1}{128}$ is compared against the following mesh sizes, $\Delta x = \frac{1}{8}$, $\frac{1}{16}$, $\frac{1}{32}$ and $\frac{1}{64}$. A basic model is created by adjusting the dimensions from the symmetric model 1 in Figure (2.2) along with a simpler set of parameters in order to find converged solutions. Such that the length of the greenhouse has been modified from 42m to 11m, and the outlet channel length has been set from 4m to 6m, however the heights and the inlet channel lengths are kept the same. Although tendencies in the magnitude of the error would change with respect to higher parameter values, for observational purposes we use a lower set of parameters, which is sufficient to evaluate the

differences and similarities between the solutions across different mesh sizes. The set of parameters used in order to find a converged solution are, $Re = 100$, $Gr = 0$, $Pr = 0.71$.

Every mesh size creates a different number of data points (x_i, y_j), such that the smaller the mesh size, the more data points created. To enforce consistency within our calculations, we sample the number of data points specified by the largest mesh $\Delta x = \frac{1}{8}$, for all the mesh sizes trialled. This results in the creation of a new data set for each mesh which corresponds to (x_i, y_j) for $\Delta x = \frac{1}{8}$. Thus the index (i, j) is assigned to the x-axis and y-axis respectively for each mesh. Equation (3.15) shows how the normalised error $E(a)$ is calculated for each variable and mesh size, where $a = \{\omega, \psi, T\}$. We take the sum of the squared difference between the solutions of a variable for the mesh size $\Delta x = \frac{1}{128}$ $\left(\widehat{S_{i,j}(a)}\right)$ from the solutions at a mesh size trialled $(S_{i,j}(a))$, by taking the data points sampled (i, j) . We then find the normalised error by dividing by the measured value.

$$E(a) = \frac{\sum_{i=0}^{N}\sum_{j=0}^{M}\left(S_{i,j}(a) - \widehat{S_{i,j}(a)}\right)^2}{\sum_{i=0}^{N}\sum_{j=0}^{M}\left(\widehat{S_{i,j}(a)}\right)^2}. \tag{3.15}$$

Table 3.2: Normalised error for vorticity (ω), stream function (ψ) and temperature (T) for each mesh size compared with mesh $\Delta x = \frac{1}{128}$.

Δx	$E(\omega)$	$E(\psi)$	$E(T)$
1/8	5.884063×10^{-3}	2.820250×10^{-5}	5.378164×10^{-4}
1/16	1.599494×10^{-3}	6.139506×10^{-6}	1.108979×10^{-4}
1/32	3.455702×10^{-4}	1.160588×10^{-6}	2.131512×10^{-5}
1/64	4.736526×10^{-5}	1.393439×10^{-7}	2.450646×10^{-6}

These values represent the error with respect to the approximated solutions from mesh size $\Delta x = \frac{1}{128}$, and so it appears that the difference in error is decaying for all variables as the mesh size is reduced. We can conclude that the finer the mesh the smaller the error for an approximated solution for each variable. In addition this convergence check highlights that there is a very small difference between the finest mesh $\Delta x = \frac{1}{128}$ and $\Delta x = \frac{1}{64}$. Despite the general concept that $\Delta x = \frac{1}{128}$ should have been applied, these calculations take a very long time, and so to achieve the best and most computationally efficient result we apply $\Delta x = \frac{1}{64}$. It is important to clarify that we cannot reduce the error in the numerical analysis at such large Reynolds number flow. Furthermore, it would be ideal to take a smaller mesh size along with an appropriate time step, however this entails a great deal of time and memory usage. Therefore we accept the error produced by $\Delta x = \frac{1}{64}$ and deem that it is adequate enough to apply throughout this project, and so $\Delta x = \Delta y = \frac{1}{64}$ has been implemented. A larger time-step of $\left(\frac{1}{64}\right)^2 \times 0.75$ has been allocated to case 1 (lower Re) where $c = 0.75$, and a smaller time-step of $\left(\frac{1}{64}\right)^2 \times 0.25$ has been used in case 2 (higher Re) where $c = 0.25$, this enforces some stability within our calculations. These simulations have been conducted using Fortran programming language.

Chapter 4

Results

We compare the symmetric (model 1) and asymmetric (model 2) channels with different fluid properties specified within each case shown in Table (4.1). Two main approaches have been taken to study the behaviour of the flow field of each model for each case. Firstly we compare models by examining the temperature field, stream function and vorticity for each case of control parameters, in order to build a greater understanding of the behaviour of the fluid. Secondly we then focus on heat balances through the temperature distributions for each model with each case to conclude whether the positioning of the outlet influences heat transfers in accordance to the different fluid properties.

Table 4.1: Specification of each case.

	Case 1	Case 2
Pr	0.71341	0.71341
Re	1.6224×10^3	1.6224×10^5
Gr	6.7696×10^5	6.7696×10^9
$\Delta x = \Delta y$	$\frac{1}{64}$	$\frac{1}{64}$
Δt	$\left(\frac{1}{64}\right)^2 \times 0.75$	$\left(\frac{1}{64}\right)^2 \times 0.25$

4.1 Comparing models

We started by comparing models by examining the temperature field $T = T(x,t)$, stream function $\psi(x,y)$ and vorticity (ω). This was to build a greater understanding of the behaviour of the fluid, as our objective is to study the fluid flow of a micro-climate within a greenhouse. We observed the state of the fluid at a moment with respect to non-dimensional time, such that we are able to monitor the variables (T, ψ, ω) at a time frame. In addition the average and variance of the field for each variable were observed using one hundred frames, given that an observation at one instantaneous time frame is not a strong enough criterion to fully understand the behaviour of the fluid flow. However, it is important we examine the fluid at a moment in order to monitor emerging patterns.

4.1.1 Temperature (T)

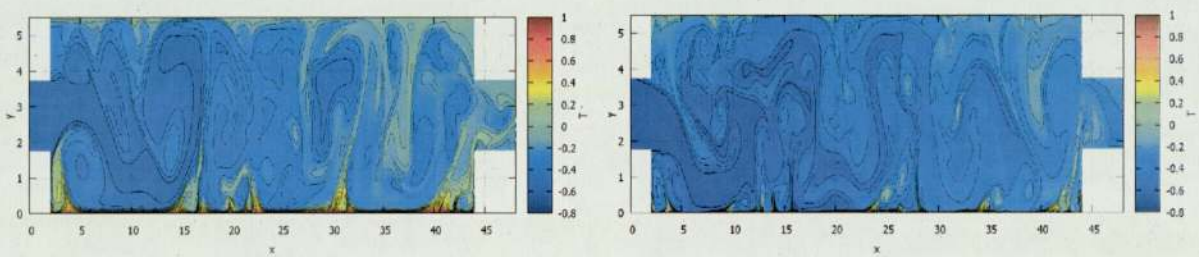

(a) (b)

Figure 4.1: Instantaneous temperature field. (a) case 1, (b) case 2. Symmetric channel (model 1).

The temperature fields for both models indicate that flows moving upstream carry cooler temperatures (darker level of blue) as ventilation is exerted from the inlet. This is further along the channel for the second case of parameters across models in Figure 4.1 (b) and Figure 4.2 (b), with respect to the horizontal direction x. In fact the furthest along is shown by the symmetric channel (model 1) at approximately $x = 27$, whereas $x = 25$ in the asymmetric channel. However it is difficult to state which model has a greater distribution of temperature. We cannot conclude whether the outlet positioning affects this upstream movement of the fluid flow, since we are looking at simply one frame at a

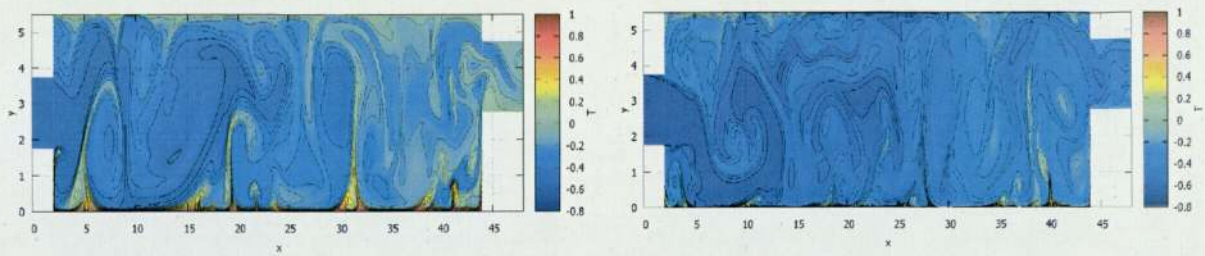

(a) (b)

Figure 4.2: Instantaneous temperature field. (a) case 1, (b) case 2. Asymmetric channel (model 2).

moment in non-dimensional time. Nevertheless, case 2 is evidently more effective in the distribution of temperature across models. In addition, in case 1 the symmetric channel (model 1) shows a better distribution of temperature to that of the asymmetric model. This may be a result of the different outlet positions, since a cooler temperature is being carried to the outlet positioning of model 1, case 1.

Moreover, the convective flows travelling from the ground to the roof occurs at irregular time intervals across cases, but similar between models respectively. For case 1, thermal convection occurs where higher levels (red) represent a hot less dense lower boundary layer that sends plumes of warm fluid upwards. The fluid rises upwards from the ground at particular positions for each model, for Figure 4.1 (a) $x = 3$, 14, 17, 23, 30 and 40, for Figure 4.2 (a) $x = 5$, 15, 19, 31, 38 and 42. Likewise the cooler fluid then moves downwards from the roof to the ground, midway between the approximated positions. The scale of the temperature near the ground for case 2 is smaller than case 1 for both models. This tells us that the properties outlined by the control parameters of case 2 are more influential in the distribution of temperature to that of case 1. Despite this observation we cannot fully understand the behaviour of the fluid flow by the temperature field at a moment, since it is irregular and changes in time. Therefore the averaged temperature field and the fluctuations from the average (variance) are observed.

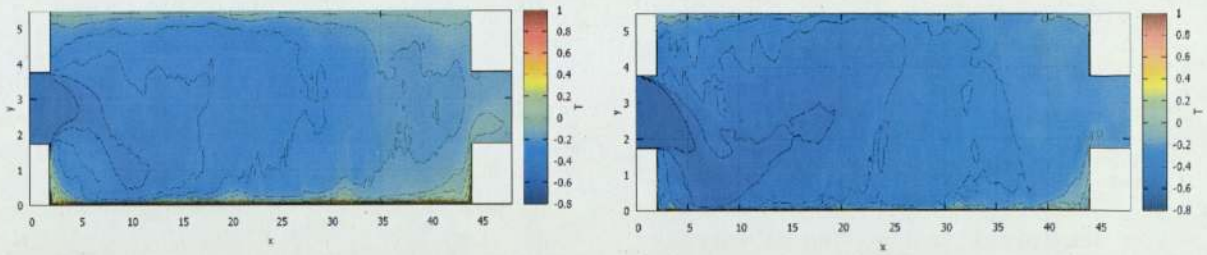

(a) (b)

Figure 4.3: Averaged temperature field. (a) case 1, (b) case 2. Symmetric channel (model 1).

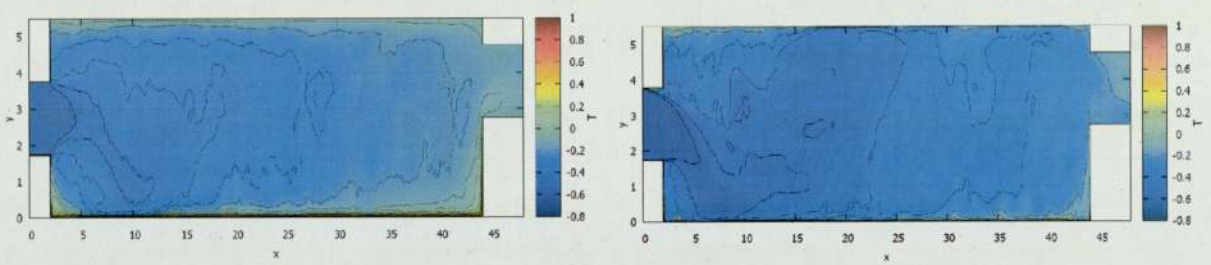

(a) (b)

Figure 4.4: Averaged temperature field. (a) case 1, (b) case 2. Asymmetric channel (model 2).

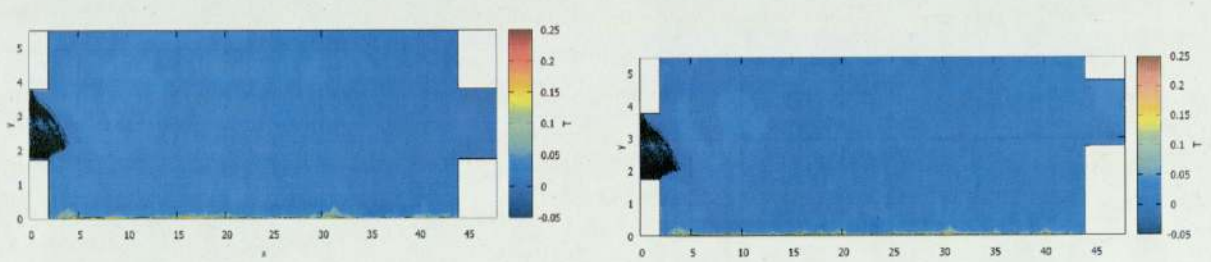

(a) (b)

Figure 4.5: Variance of temperature field. (a) Symmetric channel (model 1), (b)Asymmetric channel (model 2). Case 2

In all cases in Figure (4.3) and Figure (4.4), temperature distributions are monotonically fluctuating and decreasing in the vertical direction. When comparing cases, we can see that case 2 illustrates a higher averaged distribution of cooler temperatures, shown in Figures 4.3(b) and 4.4(b). Furthermore the symmetric channel represents a better distribution above all. On the other hand if we take the variance of the temperature field for case 2, shown in Figure (4.5), there is no distinct difference between the amplitudes of the temperature distribution. Therefore we are constricted when concluding whether the outlet position is a deciding factor. Nevertheless the comparison between cases for each model indicated that the heat in the greenhouse is indeed being swept out by ventilation and more effectively by case 2. The variance of the temperature field for the symmetric and asymmetric models for case 1 are shown in Appendix B.

4.1.1.1 Temperature profile

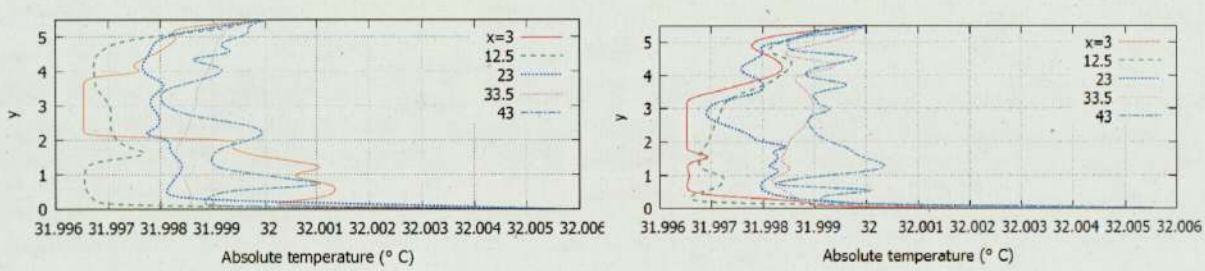

(a) (b)

Figure 4.6: Instantaneous temperature profile. $x = 3$(near inlet), 12.5, 23(middle position), 33.5, 43(near outlet). (a) Symmetric channel (model 1) , (b) Asymmetric channel (model 2). Case 1

In order to grasp a better understanding of the instantaneous temperature field, temperature profile graphs have been produced in absolute values for each case and model. As a result we are able to study the change in temperature from the inlet to the outlet. The temperature profiles are plotted with respect to the vertical direction at certain levels, $x = 3$ (near the inlet(x=2)), 12.5, 23 (the middle of the micro-climate), 33.5 and 43 (near the outlet (x=42)) in Figure (4.6) and Figure (4.7). For symmetric channel and asymmetric channel are (a) and (b) respectively. The variation between case 1 and case 2 is largely due to the great difference in the Grashof numbers (Gr) defined

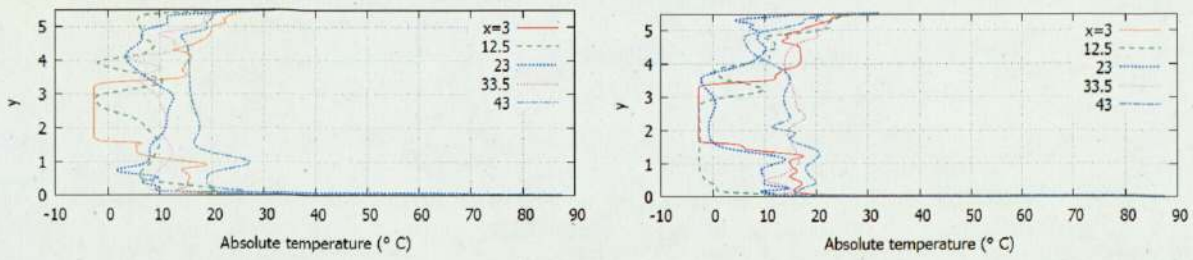

(a) (b)

Figure 4.7: Instantaneous temperature profile. $x = 3$(near inlet), 12.5, 23(middle position), 33.5, 43(near outlet). (a) Symmetric channel (model 1), (b) Asymmetric channel (model 2). Case 2

for each case, this makes it difficult to compare the different outlet positionings across cases. Therefore in order to evaluate whether the positioning of the outlet effects the distribution of temperature, we compare the symmetric channel (a) to the asymmetric channel (b) for each case.

Figure (4.6) shows that for both models the temperature change for case 1 ranges from approximately 31.9965 to 32.0055, this corresponds to the Grashof number, $Gr = 6.7696 \times 10^5$ of this particular case. Furthermore, from the derivation of the Grashof number in Equation (3.14), we were able to identify the temperature difference to be $\Delta T = 5.5427 \times 10^{-3}$. This factor is represented by the temperature profile plots, however these profiles examine the temperature at a moment and so the profiles here are very similar and there is not a distinguishing factor which differentiates the two models. Figure (4.7) compares the models for case 2, these profiles shows that the temperature ranges from -2.6419 to 87.4270, as $\Delta T = 55.427$ since $Gr = 6.7696 \times 10^9$. For case 2 the temperature difference is significantly bigger because of the higher Grashof number, this represents a buoyancy dominating effect, hence there is a bigger temperature difference.

It is difficult to highlight any significance between the two models, despite this, the temperature profiles have given us some insight into the change in temperature from the inlet to the outlet. These profiles also represent the impact the control parameters have amongst cases and clearly affects how the temperature changes within the greenhouse.

Moreover, we have seen from previous observations of the temperature field that there was some indication that case 2 may have a better temperature distribution. In addition there were signs which suggested that the symmetric channel (model 1) of case 2 showed the better distribution overall. Thus, in order to increase our understanding of the temperature field to determine which case and model is best, further analysis of the temperature field is examined later through a heat balance evaluation.

4.1.2 Stream function (ψ)

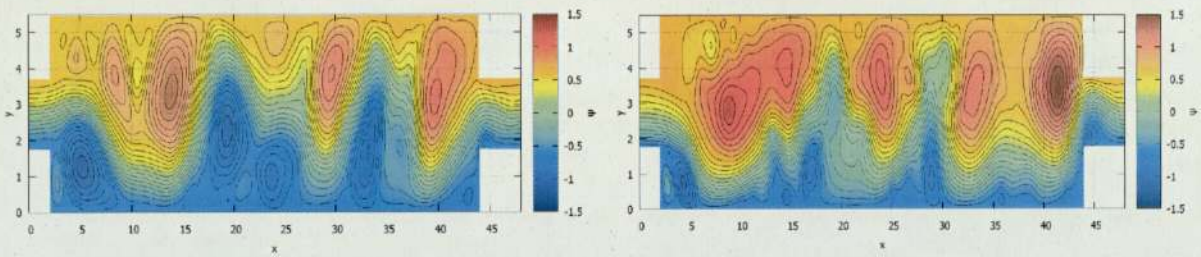

(a) (b)

Figure 4.8: Instantaneous flow pattern described by stream function. (a) case 1, (b) case 2. Symmetric channel (model 1).

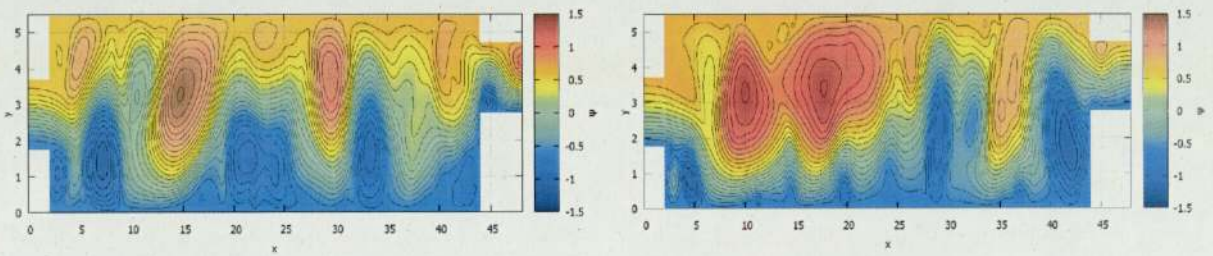

(a) (b)

Figure 4.9: Instantaneous flow pattern described by stream function. (a) case 1, (b) case 2. Asymmetric channel (model 2).

The Figures (4.8 - 4.9), display the stream functions at a moment. The streamlines are structured in a complex manner and is expressed by various re-circulating zones near the boundaries. Furthermore, between these re-circulating zones there are oscillating streamlined structures which separates the different zones. The symmetric channel shows a higher number of recirculation for case 2 seen in Figure 4.8 (b), in which the

highest volume rate of the stream function is positioned near the outlet at $x = 41$. However it is difficult to compare the fluctuations of the stream function at a moment, and so the variance is examined for a simpler aspect. The averages of the stream function for each model and case can be viewed in Appendix B.

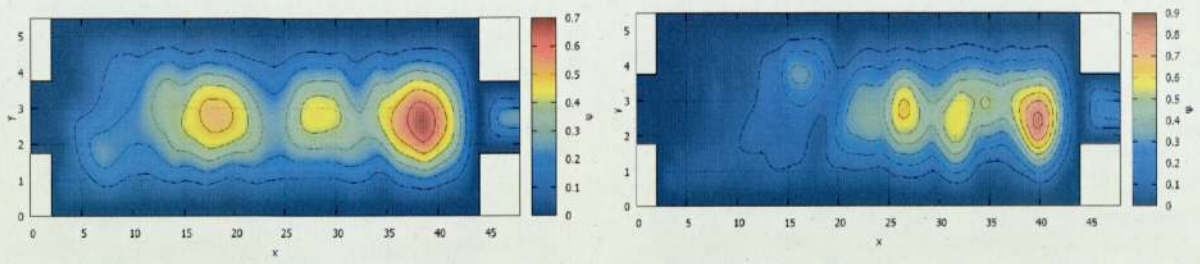

(a) (b)

Figure 4.10: Variance of stream function. (a) case 1, (b) case 2. Symmetric channel (model 1).

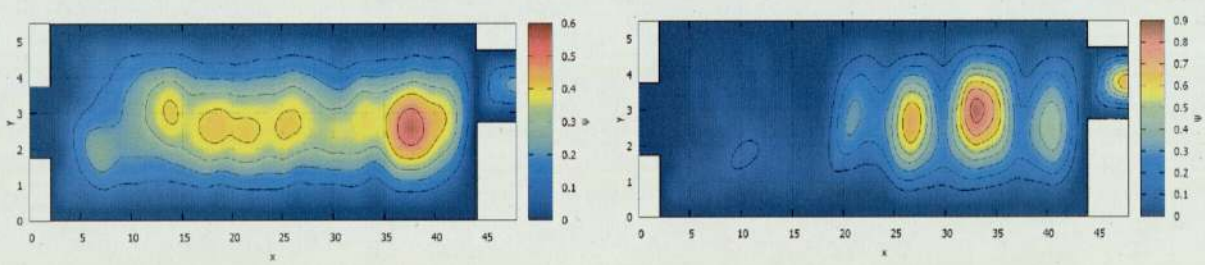

(a) (b)

Figure 4.11: Variance of stream function. (a) case 1, (b) case 2. Symmetric channel (model 2).

The fluctuations depicted by the variance shown in Figures (4.10 - 4.11), display several local maximums which signifies where the spread of the fluctuations are more dense. There are two distinct patterns between cases, since the magnitude of the stream function appears the strongest at the outlet positions for case 2 for both models, Figure 4.8 (b) and Figure 4.9 (b). In contrast, case 1 depicts the image of the stream function spread out through the channel. There are local maximums that occur in each model for each case. We deduce that for Figure 4.8 (b) there is a strong amplitude of the stream function near the outlet, but by comparing with Figure 4.9 (b), it appears

there is a higher volume rate through the outlet itself. This factor indicated that the numbers of frames taken are not enough to fully depict the behaviour of this fluid. In order to understand the thermal properties of a greenhouse we need to inspect the flow characteristics, particularly at the boundaries to comprehend these observations.

4.1.3 Vorticity(ω)

Vorticity is a measure of the local 'rotation' of the fluid particle, for which we observe the vorticity at a moment represented by Figures (4.12-4.13). Amongst all cases we can see that the concentration of vorticity is greater at the boundaries. However, we cannot derive much information from observing the overall domain, such that we focus on rotation locally around the vertical direction $0 < y \leq 1$, with respect to the horizontal direction near the ground level.

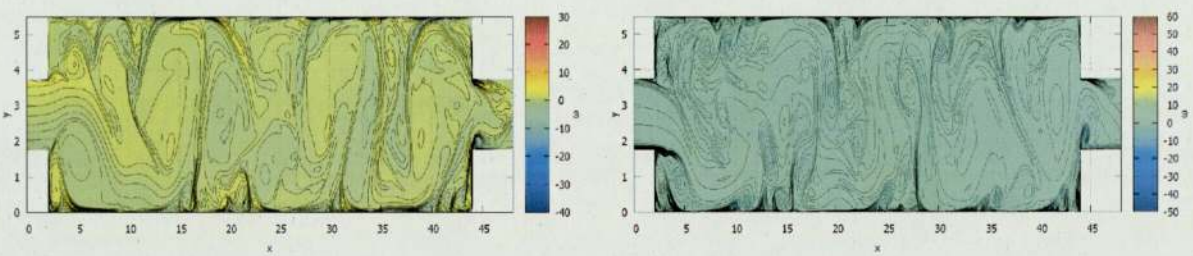

(a) (b)

Figure 4.12: Instantaneous vorticity profile. (a) case 1, (b) case 2. Symmetric channel (model 1).

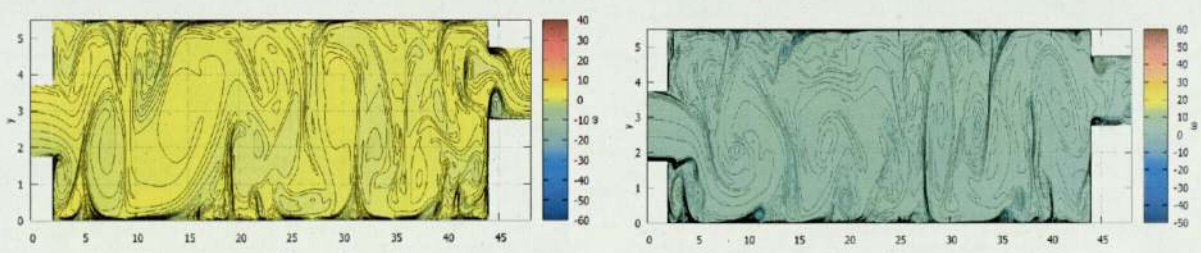

(a) (b)

Figure 4.13: Instantaneous vorticity profile . (a) case 1, (b) case 2. Asymmetric channel (model 2).

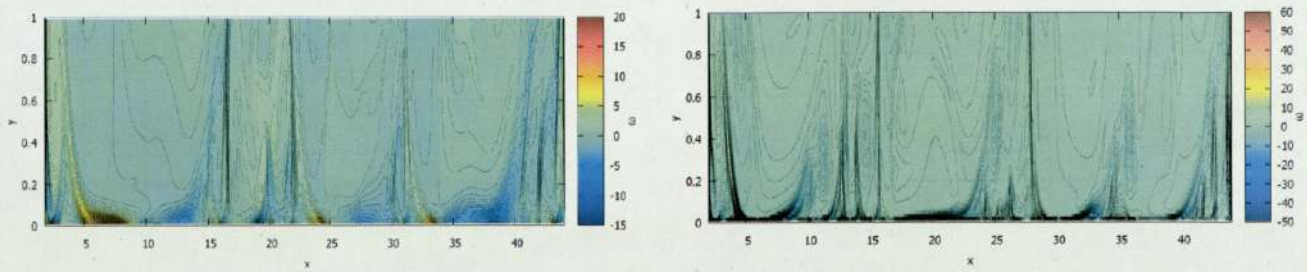

(a) (b)

Figure 4.14: Instantaneous vorticity profile at ground level. (a) case 1, (b) case 2. Symmetric channel (model 1).

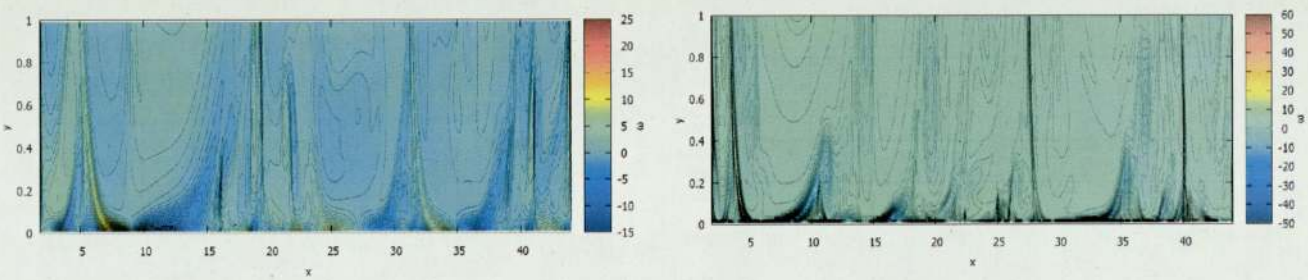

(a) (b)

Figure 4.15: Instantaneous vorticity profile at ground level. (a) case 1, (b) case 2. Asymmetric channel (model 2).

Clearly there is a larger magnitude of vorticity localised near the ground, which can seen in Figures (4.14 - 4.15). Through analysing these plots we can see that there is an alternating sign in vorticity near the ground, illustrated by the different vorticity levels. The difference in signs are represented as positive (red) and negative (blue) values. The greater level of vorticity near the ground may well be the effect from the temperature condition defined at the ground. Although we may not be able to evaluate the differences between models here, we can again see the distinction between cases. As case 2 represents a higher level of vorticity near the ground, for which we highlighted that the symmetric model shown by Figure 4.14 (b) has the most frequent measures of rotation around local vertical direction. The average and variance of vorticity are given in Appendix B.

The approach taken to understand the behaviour of the fluid flow by observing the three variables have shown us that there is a clear difference between cases. The outcome of applying a higher Reynolds number and Grashof number has shown distinctive results for each variable considered. In regards to the differentiation between models, it was apparent that the symmetric model for many instances had shown more potential in the distribution of temperature, particularly with case 2. It is important to reiterate the motivation at this stage, which is ultimately to examine the heat and mass transfer for each case to conclude which model and case is more effective. Therefore it is fair to say that these results are not sufficient to form a conclusive observation, and so we move our focus onto heat balances between models.

4.2 Heat Balance

4.2.1 Temperature distribution

In order to understand heat balances inside the greenhouse, here our focus moves to the temperature distribution. The temperature distributions are plotted with respect to the horizontal direction at certain levels $y = 0.125$ (near the ground), 1.75, 2.75 (the middle height of the greenhouse), 3.75 and 5.375 (near the roof) in Figures 4.16 and 4.17 (a) and (b). For case 1 and case 2 are (a) and (b), respectively. By selecting $N = 100$ frames of temperature fields from time series randomly an ensemble averages

$$\langle T(t,x,y)\rangle\,(x,y) \equiv \frac{1}{N}\sum_{j=1}^{N} T(t_j,x,y), \tag{4.1}$$

are evaluated instead of the ordinal time average in a period Δt:

$$\overline{T}(x,y;\Delta t) = \frac{1}{\Delta t}\int_{t_0}^{t_0+\Delta t} T(t,x,y)dt. \tag{4.2}$$

At middle positions $y = 1.75$, 2.75 and 3.75, the temperature increases monotonically

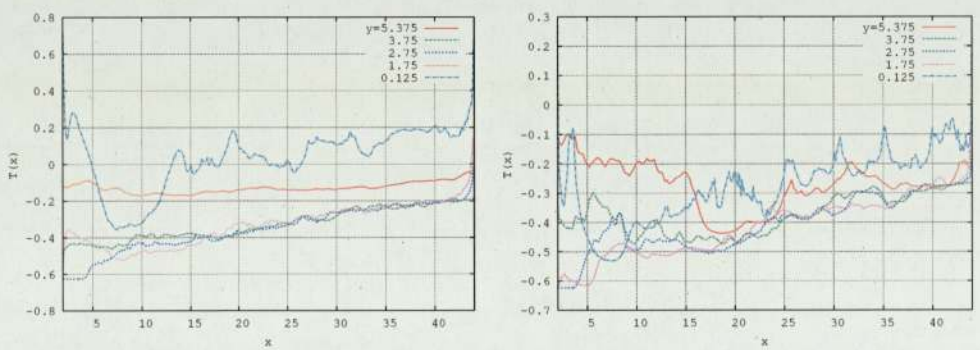

(a) (b)

Figure 4.16: Temperature distribution averaged in time. $y = 0.125$, 1.75, 2.75(middle position), 3.75, 5.375. (a) case 1, (b) case 2. Asymmetric channel (model 2).

(~ 0.008 per unit length) with respect to the x coordinate, except the inlet region where $x < 10$ in case 1, shown in Figure 4.16 (a). It is thought that the fluid is warmed from both top and bottom walls. Near the roof $y = 5.375$ the temperature distributes with -0.1, while at the outlet the temperature has positive slope. On the other hand near

the ground ($y = 0.125$) fluctuations with large amplitudes are found. Particularly near the inlet ($x < 10$) where we observed a sudden decrease of temperature. The temperature near the ground also increases as x increases, however the increased temperature leads to large fluctuations. The temperature profiles in horizontal direction for case 2 are different from case 1. Unlike case 1 the profiles are not monotonically similar, not only the ground but also the roof. In addition the distribution near the roof is also contrasting to case 1 as the fluctuations are greater, which indicated a higher level of heat transfer.

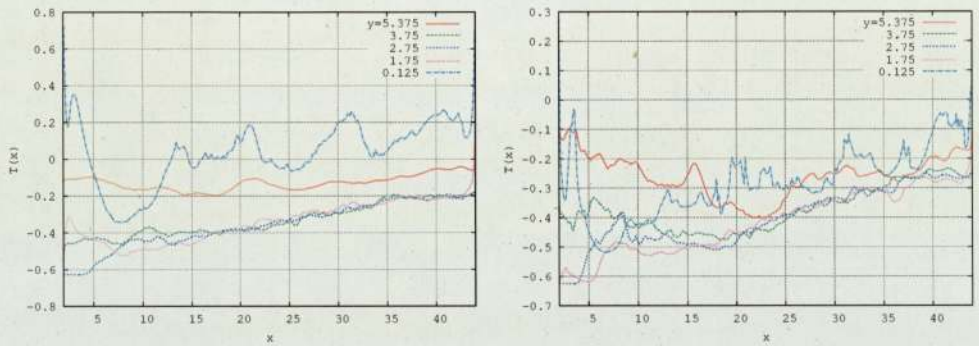

Figure 4.17: Temperature distribution averaged in time. $y = 0.125$, 1.75, 2.75(middle position), 3.75, 5.375. (a) case 1 , (b) case 2. Symmetric channel (model 1).

Figure 4.17 (a) illustrates similarly to Figure 4.16 (a) that at the middle positions $y = 1.75$, 2.75 and 3.75, the temperature increases monotonically. Furthermore by comparing these two models for case 1, it is shown that there is an almost identical level of temperature fluctuation. We examined this near the roof $y = 5.375$, as the temperature fluctuates with a similar amplitude for the symmetric channel and the asymmetric channel. In order to conclude which model brings about the greatest heat balance for each case, we examined the temperature fluctuation (variance from averaged value), and the temperature gradient at the ground and roof and arrived at the following results in Table 4.2

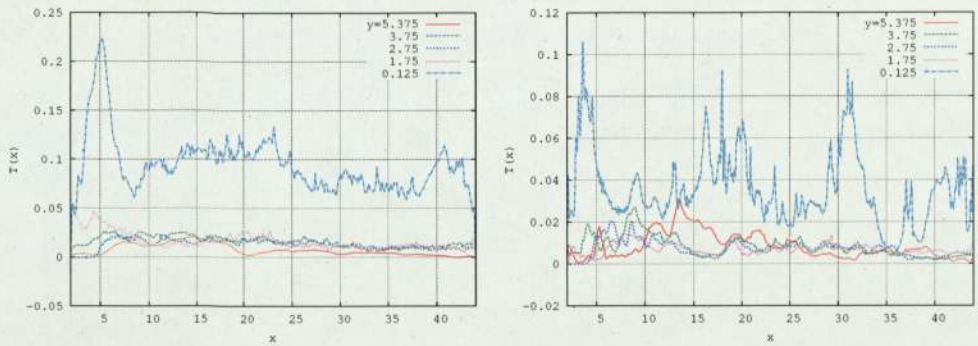

(a) (b)

Figure 4.18: Temperature fluctuation (from averaged value). (a) case 1, (b) case 2. Symmetric channel (model 1).

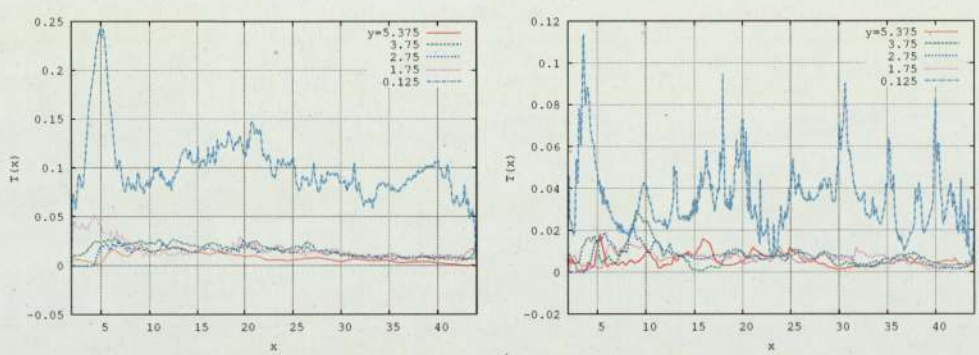

(a) (b)

Figure 4.19: Temperature fluctuation (from averaged value). (a) case 1, (b) case 2. Asymmetric channel (model 2).

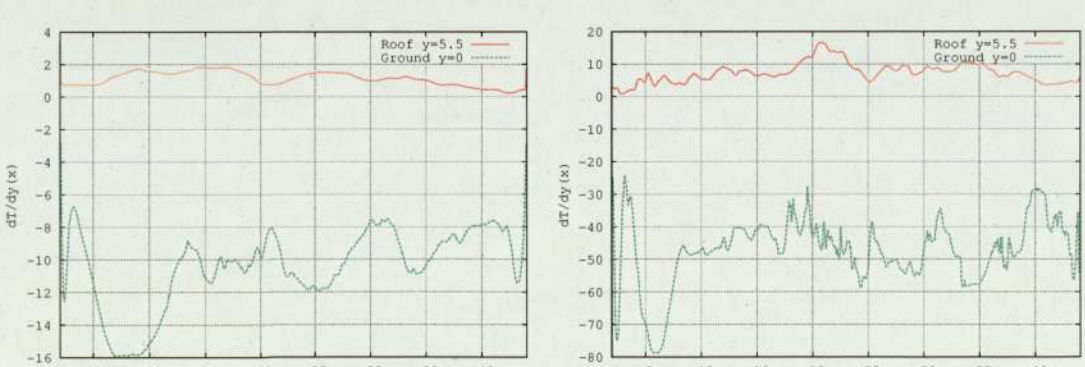

(a) (b)

Figure 4.20: Temperature gradient at ground and roof. (a) case 1, (b) case 2. Symmetric channel (model 1).

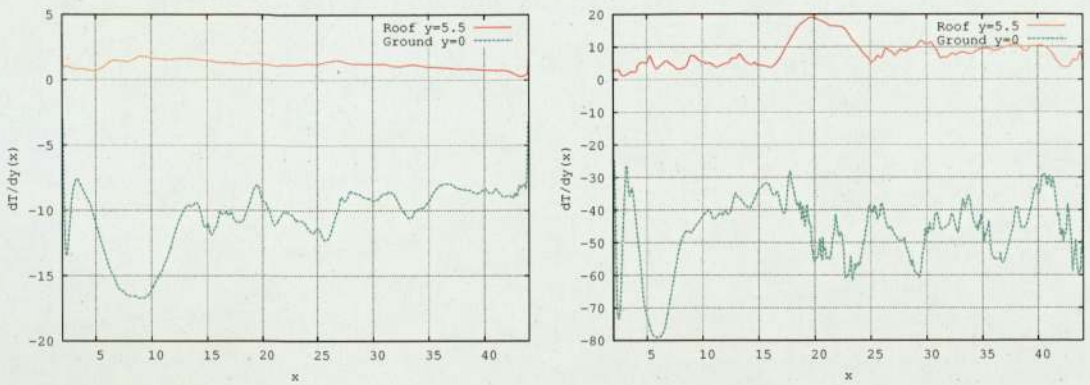

(a) (b)

Figure 4.21: Temperature gradient at ground and roof. (a) case 1, (b) case 2. Asymmetric channel (model 2).

Table 4.2: Temperature gradient $\overline{-\frac{\partial T}{\partial n}}$ for average of time dependent flow field and the temperature fluctuation of the flow field ($\widetilde{\frac{\partial T}{\partial n}}$)

Model	Ground	Roof
Symmetric channel (model 1). Case 1.	10.36 (0.333)	1.20 (0.0183)
Symmetric channel (model 1). Case 2.	47.35 (7.560)	7.55 (0.387)
Asymmetric channel (model 2). Case 1.	10.49 (0.363)	1.24 (0.0203)
Asymmetric channel (model 2). Case 2.	46.67 (7.366)	8.31 (0.316)

4.2.2 Evaluation of heat balance

Heat flux is defined as the amount of heat transferred per unit area per unit time through a given surface. Fourier's law states the following,

$$\text{Heat transfer} \propto (\text{temperature difference})$$

$$\propto (\text{area normal to direction of heat flow})$$

giving the relationship

$$\boldsymbol{q} = -\lambda \frac{\partial T}{\partial \boldsymbol{n}}, \tag{4.3}$$

where $\boldsymbol{q}$ is the heat flux, $\frac{\partial T}{\partial \boldsymbol{n}}$ is the temperature gradient with $\boldsymbol{n}$ a unit vector normal to the wall (surface), λ is a thermal conductivity constant. We have derived the following temperature gradient, $\overline{-\frac{\partial T}{\partial n}}$ for the average of time dependent flow field which represents the heat flux for each wall. We use this to evaluate the heat balances within each model for each case.

Suppose a simple case where there is no buoyancy effect and no convection on the flow field, there then exists a ratio of the averaged temperature gradient with respect to time and space between the ground and roof (q_g:q_r), as (2.6 : 1). This ratio refers to how effective ventilation is in removing the heat with respect to the ground. We evaluated heat balances for each model by calculating this ratio for the cases we have defined through the different sets of parameters. Additionally, the total heat flux from both walls, ground (q_g) and roof (q_r) is considered to identify the magnitude of how much heat has been swept out by ventilation such that

$$Q = (q_g) + (q_r).$$

Table 4.3: Ratio of the average temperature gradient, (q_g:q_r) and total heat flux (Q) from both walls

Model	Ratio of averaged gradient	Total heat flux
Symmetric channel (model 1). Case 1.	8.633 : 1	11.56
Symmetric channel (model 1). Case 2.	6.272 : 1	54.90
Asymmetric channel (model 2). Case 1.	8.460 : 1	11.73
Asymmetric channel (model 2). Case 2.	5.616 : 1	54.98

These results are shown in Table (4.3) and it appears that the ratio of the averaged gradient was larger in case 1 where the properties of the fluid are defined by a lower Reynolds number ($Re = 1.6224 \times 10^3$) and lower Grashof number ($Gr = 6.7696 \times 10^5$). Moreover this ratio refers to the removal of heat at the ground, effectively more than the roof in case 1 across the symmetric channel (model 1) and asymmetric channel (model 2), rather than case 2. However this does not necessarily represent greater levels of ventilation, therefore the magnitude of the heat being swept out by ventilation was considered through the evaluation of the total heat flux (Q.)

We can see clearly from Table (4.3) that the largest total heat flux is far greater in case 2 across models, where the properties of the fluid are defined by a higher Reynolds number ($Re = 1.6224 \times 10^5$) and higher Grashof number ($Gr = 6.7696 \times 10^9$). This suggests that case 2 was evidently a better set of control parameters to sweep out greater amounts of heat by ventilation. We determined from all forms of the evaluation of heat balances that the symmetric channel for the set of parameters defined by case 2 is best for the ventilation of our modelled micro-climate. With a total heat flux of $Q = 54.90$ and a ratio of averaged gradient between the ground and the roof is $6.272 : 1$.

Chapter 5

Conclusions and future work

5.1 Conclusions

The aim of this research project was to amend the conditions of a micro-climate to remove heat by ventilation, as well as to determine which model is ventilated better by comparing models across cases. This was achieved by comparing models for each case through evaluating heat balances, which built a better understanding of the behaviour of the fluid flow. Additionally by observing the temperature field, stream function and vorticity of the fluid flow, we have come to the conclusion that the symmetric channel (model 1) achieved the best distribution of temperature for both cases, for which case 2 became the better set of fluid properties.

It became apparent during our investigation that the difference between the cases were greatly influenced by the values of the control parameters and was ultimately the deciding factor in the study of heat balances. The second case was highlighted as the more effective case in the study of ventilation, given that the higher Reynolds and Grashof numbers were $Re = 1.6224 \times 10^5$, and $Gr = 6.7696 \times 10^9$, respectively, compared to the lower parameter values of case 1, $Re = 1.6224 \times 10^3$, and $Gr = 6.7696 \times 10^5$. It is important to highlight the significance of these control parameters, the Reynolds number is derived from the ratio between inertial forces to viscous forces, and so a higher Reynolds number would in effect represent a fluid in which inertial forces are dominant

(lower viscosity) and a faster flowing fluid. Additionally the buoyancy effect of the higher Grashof number enhances heat transfer, as the derivation of the Grashof number signifies the ratio between buoyancy forces to viscous forces.

Despite comparing the models for each case separately, there has been no a distinguishing factor between the symmetric and asymmetric channels for each case specific. The models have exhibited very similar characteristics in the behaviour of fluid flows when observing the different channels within the same case, although there has been some indication that the symmetric channel is better ventilated. Moreover, by the examining heat balances, there has been more evidence of this, and we were able to conclude that the best efficiency could be achieved by the symmetric model for case 2. This has been validated by the evaluation of heat balances and determined by a total heat flux of $Q = 54.90$ with a ratio of nondimensional heat flux averaged in time between the ground and the roof as $6.272 : 1$. The outcome of this research suggests that the values of the control parameters are the most effective factors in this study of heat balances within a greenhouse.

5.2 Future work

The work of this project could be further investigated in the following ways.

- Exploring different values of control parameters to create additional cases to distinguish which of the two models (symmetric and asymmetric channels) is more effective in the ventilation of a micro-climate.

- Application of different models created by re-positioning the outlet near the ground, furthermore the introduction of multiple outlets may be a viable option to improve the ventilation of a micro-climate.

- The basis of the research conducted has been upon the temperature distribution and ventilation rate, this could be expanded by considering another factor, such as the change in humidity between models for each case.

- The progression to a three-dimensional analysis of the micro-climate of the greenhouse to investigate how temperature conditions are to be maintained through ventilation. This study would be of great interest to identify how to provide better conditions to cultivate crops within a greenhouse in the UAE.

Bibliography

Böer, B. (1997). An introduction to the climate of the united arab emirates. *Journal of Arid Environments 1*(35), 3–16.

Boussinesq, J. (1903). Théorie analytique de la chaleur. *Gauthier-Villars, Paris 2.*

Croft, D. R. and D. G. Lilley (1977). Heat transfer calculations using finite different equations. pp. 1–32.

Davies, P. A. (2005). A solar cooling system for greenhouse food production in hot climates. *Solar Energy 79*, 661–668.

Davies, P. A. and C. Paton (2005). The seawater greenhouse in the united arab emirates: thermal modelling and evaluation of design options. *Desalination 173*, 103 –111.

Doering, C. R. and J. D. Gibbon (1995). Applied analysis of the navier-stokes equation. pp. 1–17.

Foias, C., O. Manley, R. Rosa, and R. Temam (2001). Navier-stokes equations and turbulence. pp. 1–25.

Kumar, K. S., K. N. Tiwari, and K. J. Madan (2009). Design and technology for greenhouse cooling in tropical and subtropical regions: A review. *Energy Buildings 12*(41), 1269– 1275.

Loukopoulos, V., G. Messaris, and G. Bourantas (2013). Numerical solution of the incompressible navier-stokes equations in primitive variables and velocity-vorticity formulation. *Applied Mathematics and Computation. 222*(1), 575–588.

Sapounas, A. A., T. Bartzanas, C. Nikita-Martzopoulou, and C. Kittas (2008). Aspects of cfd modelling of a fan and pad evaporative cooling system in greenhouses. *The International Journal of Ventilation 4*(6), 379–388.

Sethi, V. P. and S. K. Sharma (2007). Survey of cooling technologies for worldwide agricultural greenhouse applications. *Solar Energy 21*(81), 1447–1459.

Torre-Gea, G. D. L., G. M. Soto-Zarazúa, and I. López-Crúz (2011). Computational fluid dynamics in greenhouses: A review. *African Journal of Biotechnology 77*(10), 17651–17662.

Zabeltitz, C. V. (2011). Integrated greenhouse systems for mild climates: Climate conditions, design, construction, maintenance, climate control. pp. 5–6.

Zeytounian, R. K. and C. R. Mecanique (2003). Joseph boussinesq and his approximation: A contemporary view. *Comptes Rendus Mecanique 8*(331), 575–586.

Appendices

Appendix A

Nondimensionalisation of Navier-Stokes equation

The following are basic equations used in this project,

General Navier Stokes momentum equation

$$\rho\left[\frac{\partial \boldsymbol{u}}{\partial t}+(\boldsymbol{u}\cdot\nabla)\,\boldsymbol{u}\right]=-\nabla p+\mu\nabla^2\boldsymbol{u}-\rho\boldsymbol{g}. \tag{A.1}$$

Dimensional Navier-Stokes momentum equation

$$\rho_0\left[\frac{\partial \boldsymbol{u}}{\partial t}+(\boldsymbol{u}\cdot\nabla)\,\boldsymbol{u}\right]=-\nabla p+\mu\nabla^2\boldsymbol{u}+g\gamma T\hat{\boldsymbol{j}}. \tag{A.2}$$

Nondimensional Navier-Stokes momentum equation

$$\frac{\partial \boldsymbol{u}^*}{\partial t^*}+(\boldsymbol{u}^*\cdot\nabla^*)\boldsymbol{u}^*=-\nabla^* p*+\frac{1}{Re}\nabla^{*^2}\boldsymbol{u}^*+\frac{Gr}{(Re)^2}T^*\,\hat{\boldsymbol{j}}. \tag{A.3}$$

Dimensional incompressibility condition

$$\nabla\cdot\boldsymbol{u}=0. \tag{A.4}$$

Nondimensional incompressibility condition

$$\nabla^* \cdot \boldsymbol{u}^* = 0. \tag{A.5}$$

Dimensional energy equation

$$\frac{\partial T}{\partial t} + (\boldsymbol{u} \cdot \nabla) T = \kappa \nabla^2 T. \tag{A.6}$$

Nondimensional energy equation

$$\frac{\partial T^*}{\partial t^*} + (\boldsymbol{u}^* \cdot \nabla^*) T^* = \frac{1}{Pr\, Re} \nabla^{*^2} T^*. \tag{A.7}$$

A.1 Normalisation of parameters

We normalise every parameter by substituting for every dimensional parameter to nondimensionalise.

Table A.1: Normalised parameters.

Parameter	**Nondimensional**	**Dimensional**
Time Scale (t)	$t^* = \frac{U}{L} t$	$t = \frac{L}{U} t^*$
Time Derivation $\left(\frac{\partial}{\partial t}\right)$	$\frac{\partial}{\partial t^*} = \frac{L}{U} \frac{\partial}{\partial t}$	$\frac{\partial}{\partial t} = \frac{U}{L} \frac{\partial}{\partial t^*}$
Pressure (p)	$p^* = \frac{p}{\rho U^2}$	$p = p^* \rho U^2$
Nabla (∇)	$\nabla^* = L \nabla$	$\nabla = \frac{1}{L} \nabla^*$
Velocity Vector ($\boldsymbol{u}$)	$\boldsymbol{u}^* = \frac{\boldsymbol{u}}{U}$	$\boldsymbol{u} = U \boldsymbol{u}^*$
Temperature ($T - Tr$)	$T^* = \frac{T - Tr}{Tg - Tr}$ *and* $\Delta T = Tg - Tr$	$T - Tr = T^* \Delta T$

A.1.1 Nondimensional momentum equation

We begin by taking the dimensional momentum equation from Equation (A.2) and using the normalised parameters in Table (A.1)

$$\frac{\partial(U\boldsymbol{u}^*)}{\partial\left(\frac{Lt^*}{U}\right)} + \left(U\boldsymbol{u}^* \cdot \frac{\nabla^*}{L}\right) U\boldsymbol{u}^* = \frac{-\nabla^* p}{\frac{L}{\rho}} + g\alpha(T - Tr)\hat{\boldsymbol{j}} + \nu\frac{\nabla^{*^2}}{L^2}(U\boldsymbol{u}^*), \tag{A.8}$$

$$\left(\frac{U^2}{L}\right)\frac{\partial \boldsymbol{u}^*}{\partial t^*} + \left(\frac{U^2}{L}\right)(\boldsymbol{u}^* \cdot \nabla^*)\boldsymbol{u}^* = \frac{-\nabla p}{L\rho} + \frac{\mu}{\rho}\frac{U}{L^2}(\nabla^{*^2}\boldsymbol{u}^*) + g\gamma(T - Tr)\hat{\boldsymbol{j}}. \tag{A.9}$$

Multiplying Equation (A.9) by $\frac{L}{U^2}$ hence:

$$\frac{\partial \boldsymbol{u}^*}{\partial t^*} + (\boldsymbol{u}^* \cdot \nabla^*)\boldsymbol{u}^* = \underbrace{\nabla^* \frac{-p}{\rho U^2}}_{(1)} + \underbrace{\frac{\mu}{\rho U L}\nabla^{*^2}\boldsymbol{u}^*}_{(2)} + \underbrace{\frac{g\gamma(T - Tr)L\hat{\boldsymbol{j}}}{U^2}}_{(3)}. \tag{A.10}$$

Now solving each term on the R.H.S

- Label **(1)**.

  Substituting for p^* as given in Table (A.1). Therefore Label **(1)** becomes

$$\nabla^* \frac{-p}{\rho U^2} = -\nabla^* p^*. \tag{A.11}$$

- Label **(2)**.

  Given that $Re = \frac{\rho UL}{\mu}$. Therefore Label **(2)** becomes

$$\frac{\mu}{\rho UL}\nabla^{*2}\boldsymbol{u}^* = \frac{1}{Re}\nabla^{*^2}\boldsymbol{u}^*. \tag{A.12}$$

- Label **(3)**.

  Given that $Gr = \frac{g\gamma\Delta TL^3}{\nu^2}$ and $Re = \frac{\rho UL}{\mu}$m, therefore by substituting for T^* as given in Table (A.1), Label **(3)** becomes,

$$\frac{g\gamma(T - Tr)L\hat{\boldsymbol{j}}}{U^2} = \left[\frac{g\gamma\Delta TL}{U^2}\right] T^*\hat{\boldsymbol{j}}, \tag{A.13}$$

$$= \frac{Gr}{(Re^2)} T^*\hat{\boldsymbol{j}}. \tag{A.14}$$

Thus putting Equations (A.11) (A.12) (A.14) into (A.10) the Navier Stokes nondimensional momentum equation is derived,

$$\frac{\partial \boldsymbol{u}^*}{\partial t^*} + (\boldsymbol{u}^* \cdot \nabla^*)\boldsymbol{u}^* = -\nabla^* p* + \frac{1}{Re}\nabla^{*^2}\boldsymbol{u}^* + \frac{Gr}{(Re)^2} T^* \hat{\boldsymbol{j}}. \tag{A.15}$$

A.1.2 Nondimensional incompressibility condition

Substituting the normalized parameters form the Table (A.1) into Equation (A.4), we derive the following nondimensional incompressibility condition:

$$\left(\frac{\nabla^*}{L}\right) \cdot (U\boldsymbol{u}^*) = 0, \tag{A.16}$$

$$\frac{U}{L}(\nabla^* \cdot \boldsymbol{u}^*) = 0, \tag{A.17}$$

$$\nabla^* \cdot \boldsymbol{u}^* = 0. \tag{A.18}$$

A.1.3 Nondimensional energy equation

Given $Pr = \frac{\nu}{\kappa}$, by substituting the dimensional parameters as given in Table (A.1), equation (A.6) becomes

$$\frac{\partial(\Delta T T^*)}{\partial\left(\frac{L}{U}\right)t^*} + \left(U\boldsymbol{u}^* \cdot \frac{\nabla^*}{L}\right)\Delta T T^* = \frac{\kappa\nabla^{*^2}}{L^2}\Delta T T^*, \tag{A.19}$$

$$\frac{L\Delta T}{U}\frac{\partial T^*}{\partial t^*} + \frac{L\Delta T}{U}(\boldsymbol{u}^* \cdot \Delta^*)T^* = \frac{\Delta T}{L^2}\kappa\nabla^{*^2}T^*, \tag{A.20}$$

$$\frac{\partial T^*}{\partial t^*} + (\boldsymbol{u}^* \cdot \nabla^*)T^* = \frac{\kappa}{UL}\nabla^{*^2}T^*. \tag{A.21}$$

Multiplying the R.H.S of Equation (A.21) by $\frac{\nu}{\nu}$, hence

$$\frac{\partial T^*}{\partial t^*} + (\boldsymbol{u}^* \cdot \nabla^*)T^* = \frac{\kappa}{\nu}\frac{\nu}{UL}\nabla^{*^2}T^*, \tag{A.22}$$

such that we determine the nondimensional energy equation

$$\frac{\partial T^*}{\partial t^*} + (\boldsymbol{u}^* \cdot \nabla^*)T^* = \frac{1}{PrRe}\nabla^{*^2}T^*. \tag{A.23}$$

Appendix B

Temperature, stream function and vorticity plots

In chapter 4 we compared the symmetric channel and the asymmetric channels (models) across the two parameter sets, case 1 and case 2 by examining the temperature field ($T = T(x,t)$), stream function ($\psi(x,y)$) and vorticity (ω). The following are the remaining plots for each variable.

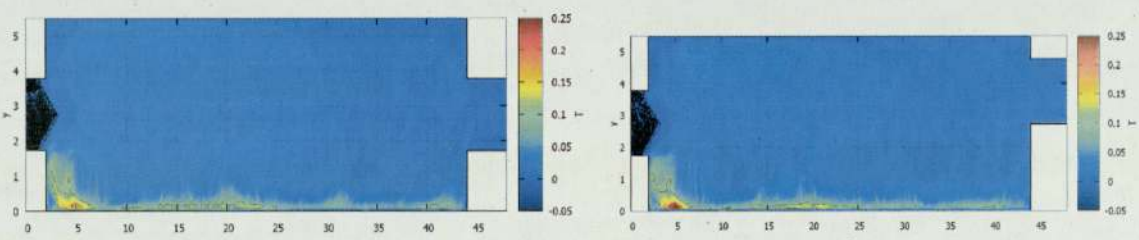

(a) (b)

Figure B.1: Variance of temperature field. (a) Symmetric channel (model 1), (b) Asymmetric channel (model 2), case 1 .

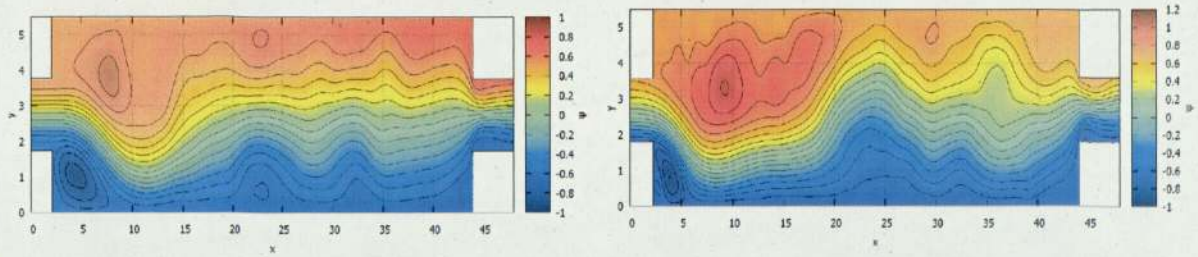

(a) (b)

Figure B.2: Average of stream function. (a) case 1, (b) case 2. Symmetric channel (model 1).

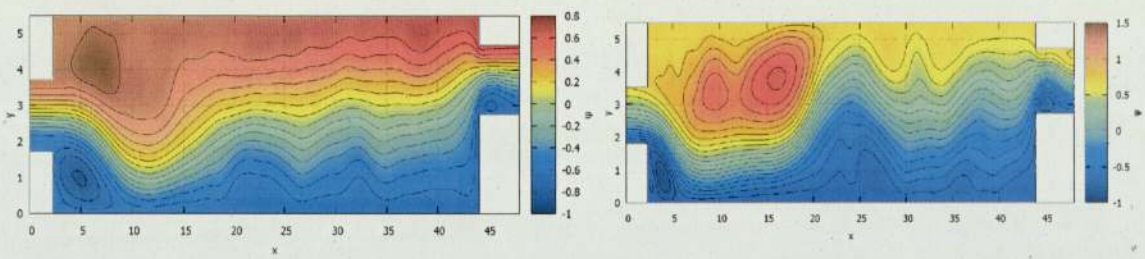

(a) (b)

Figure B.3: Average of stream function. (a) case 1, (b) case 2. Asymmetric channel (model 2).

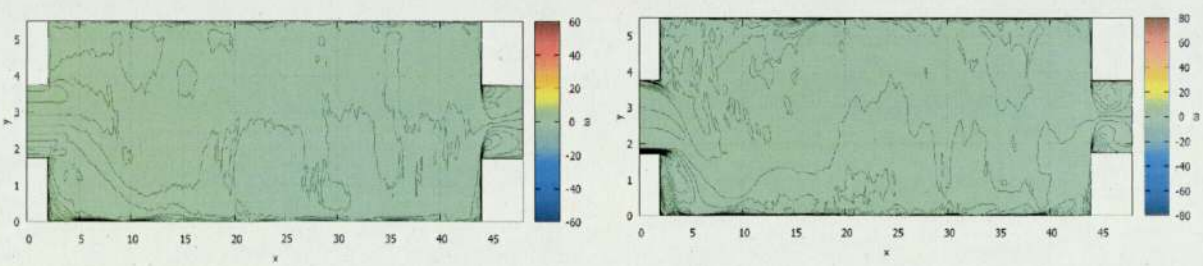

(a) (b)

Figure B.4: Average of vorticity. (a) case 1, (b) case 2. Symmetric channel (model 1).

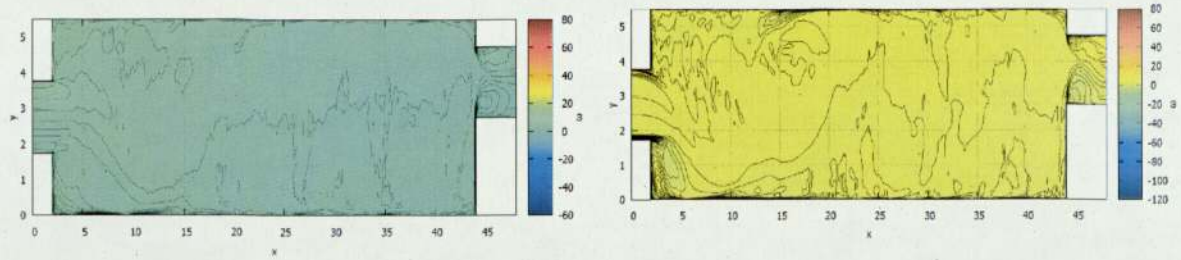

(a) (b)

Figure B.5: Average of vorticity. (a) case 1, (b) case 2. Asymmetric channel (model 2).

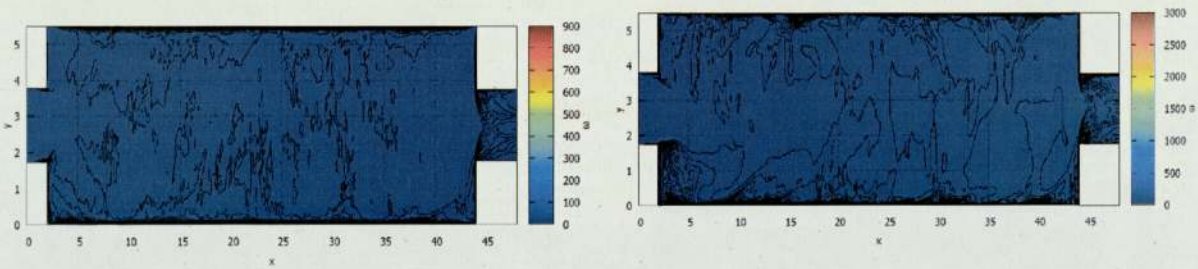

(a) (b)

Figure B.6: Variance of vorticity. (a) case 1, (b) case 2. Symmetric channel (model 1).

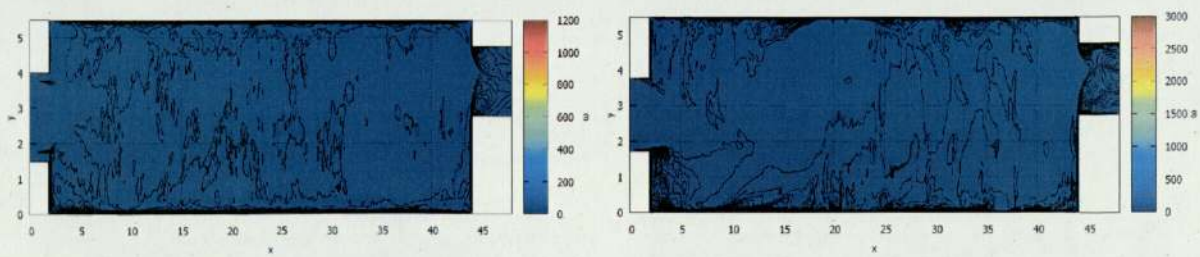

(a) (b)

Figure B.7: Variance of vorticity. (a) case 1, (b) case 2. Asymmetric channel (model 2).